SUPPLEMENTARY INFORMATION

Altermagnetism: spin-momentum locked phase protected by non-relativistic symmetries

Libor Šmejkal,[1,2] Jairo Sinova,[1,2] and Tomas Jungwirth[2,3]

[1]*Institut für Physik, Johannes Gutenberg Universität Mainz, 55128 Mainz, Germany*

[2]*Institute of Physics, Czech Academy of Sciences, Cukrovarnická 10, 162 00, Praha 6, Czech Republic*

[3]*School of Physics and Astronomy, University of Nottingham, NG7 2RD, Nottingham, United Kingdom*

CONTENTS

I. DETAILS OF THE DERIVATION OF SPIN GROUP CATEGORIZATION OF NON-RELATIVISTIC COLLINEAR MAGNETISM

The first type of the non-trivial spin Laue groups is obtained from the group of spin-space transformations $\mathbf{S}_1 = \{E\}$ whose only possible coset decomposition contains one coset, which is $\mathbf{S}_1$ itself. The corresponding isomorphic one-coset decomposition of a crystallographic Laue group $\mathbf{G}$ is, therefore, again $\mathbf{G}$ itself. As a result, the first type of non-trivial spin Laue groups is given by $\mathbf{R}_s^{\mathrm{I}} = [E \parallel \mathbf{G}]$.

The second type of the non-trivial spin Laue groups is obtained from the one-coset decomposition of $\mathbf{S}_2 = \{E, C_2\}$, i.e., $\mathbf{S}_2$ itself. The corresponding non-trivial spin Laue groups are then given by $\mathbf{R}_s^{\mathrm{II}} = [E \parallel \mathbf{G}] + [C_2 \parallel \mathbf{G}]$. Below we will show that the $\mathbf{R}_s^{\mathrm{II}}$ groups also describe Kramers spin-degenerate collinear antiferromagnetism in crystals with the opposite-spin-sublattice transformation symmetry $[C_2 \parallel \bar{E}]$, where $\bar{E}$ on the right side of the double vertical bar is the real-space inversion.

Since $\mathbf{S}_2$ has two elements, its only additional coset decomposition contains two cosets,

$\mathbf{S}_2 = \{E\} + C_2\{E\}$. The corresponding isomorphic two-coset decomposition of the crystallographic Laue group is given by, $\mathbf{G} = \mathbf{H} + A\mathbf{H} = \mathbf{H} + (\mathbf{G} - \mathbf{H})$, where $\mathbf{H}$ is a halving subgroup of $\mathbf{G}$ and A is any chosen element of $\mathbf{G} - \mathbf{H}$. The non-trivial spin Laue groups obtained from this coset decomposition take a form,

$$\mathbf{R}_s^* = [E \parallel \mathbf{H}] + [C_2 \parallel A]\,[E \parallel \mathbf{H}] = [E \parallel \mathbf{H}] + [C_2 \parallel \mathbf{G} - \mathbf{H}]. \tag{1}$$

We see from Eq. (1) that for $\mathbf{R}_s^*$, $\mathbf{G}$ is expressed as a sublattice coset decomposition, where $\mathbf{H}$ contains only the real-space transformations which interchange atoms between same-spin sublattices, and $\mathbf{G}-\mathbf{H}$ contains only the real-space transformations which interchange atoms between opposite-spin sublattices.

Because of the symmetry $[\bar{C}_2 \parallel \mathcal{T}]$ of the collinear spin arrangements, following from their spin-only group, and because $[\bar{C}_2 \parallel \mathcal{T}]$ acts the same on $\epsilon(s, \mathbf{k})$ as $[E \parallel \bar{E}]$, the latter is also a symmetry of all non-relativistic collinear magnets. This turns Eq. (1) in two distinct types, depending on whether the real-space inversion is an element of $\mathbf{G} - \mathbf{H}$, i.e. belongs to the opposite-spin-sublattice transformations, or is an element of $\mathbf{H}$, i.e. belongs to the same-spin-sublattice transformations. In the former case, $[E \parallel \bar{E}][E \parallel \mathbf{H}] = [E \parallel \mathbf{G}]$, and $\mathbf{R}_s^*$ becomes $\mathbf{R}_s^{\mathrm{II}}$. This explains the above statement that the $\mathbf{R}_s^{\mathrm{II}}$ Kramers spin-degenerate antiferromagnetic phase is also obtained when the real-space inversion interchanges atoms between opposite-spin sublattices.

In the other case when the real-space inversion is an element of $\mathbf{H}$, $[E \parallel \bar{E}][E \parallel \mathbf{H}] = [E \parallel \mathbf{H}]$, and we arrive at the remaining third distinct type of the non-trivial spin Laue groups, $\mathbf{R}_s^{\mathrm{III}}$. It is given by Eq. (1) with A representing a real-space proper or improper rotation which interchanges atoms between opposite-spin sublattices.

II. MODEL $\mathbf{k}\cdot\mathbf{p}$ HAMILTONIANS OF ALTERMAGNETS

The six model $\mathbf{k}\cdot\mathbf{p}$ Hamiltonian bands in Tab. 1 in the main text, representing planar (P) and bulk (B) altermagnetic spin-momentum locking with the spin winding number $W = 2$, 4, and 6 around the $\mathbf{\Gamma}$-point, are given by

$$H_{P-2,d} = Jk_xk_y, \tag{2}$$

$$H_{P-4,g} = Jk_xk_y(k_x^2 - k_y^2), \tag{3}$$

$$H_{P-6,i} = Jk_xk_y\left((\sqrt{3}k_x)^2 - k_y^2\right)\left((\sqrt{3}k_y)^2 - k_x^2\right), \tag{4}$$

which are independent of k_z, and by

$$H_{B-2,d} = Jk_zk_x, \tag{5}$$

$$H_{B-4,g} = Jk_zk_x\left(k_x^2 - \left(\sqrt{3}k_y\right)^2\right), \tag{6}$$

$$H_{B-6,i} = J\left(k_x^2 - k_y^2\right)\left(k_y^2 - k_z^2\right)\left(k_z^2 - k_x^2\right). \tag{7}$$

which are k_z-dependent. Here J is the strength of the spin splitting and d, g, and i refer to the d-wave, g-wave, and i-wave anisotropic crystal harmonic symmetry. The previously reported materials and models[1–19] belong the the $H_{P-2,d}$ class.

III. SPIN SPLITTING BY ELECTRIC CRYSTAL FIELD AND COMPARISON TO RELATIVISTIC MAGNETIC GROUPS AND DFT CALCULATIONS FOR RuO_2

We start by illustrating the difference between the spin group and the magnetic group of RuO_2. In Supplementary Fig. S1a we give the spin group of altermagnetic RuO_2, $2_4/1_m1_m1_m$. We also explicitly indicate the generators $[E \parallel M_i]$, where M_i are the three orthogonal mirror planes, of the same-spin-sublattice transformations (black), and the generator $[C_2 \parallel C_{4z}]$ of the opposite-spin-sublattice transformations (red).

In Supplementary Fig. S1c we give the magnetic group $m'm'm$ for the magnetic moment vectors along the [110]-axis shown in the panel by purple and cyan arrows. We include also its generators which are one mirror plane orthogonal to the magnetic moments (black) and two mirror planes parallel to the moments combined with time-inversion (blue). We highlight that all these symmetry elements are same-spin-sublattice transformations and that the magnetic group contains no opposite-spin-sublattice transformation elements. We also point out that two of the same-spin-sublattice mirror transformations are combined with the time-inversion, while the third one is not combined with the time-inversion. In general, magnetic group symmetries can have same-spin-sublattice transformations with or without

time-inversion, and opposite-spin-sublattice transformations with or without time-inversion. This contrasts with the sublattice coset decomposition form of all altermagnetic $\mathbf{R}_s^{\mathrm{III}}$ spin groups, whose elements are divided into the same-spin-sublattice transformations $[E \parallel \mathbf{H}]$ and the opposite-spin-sublattice transformations $[C_2 \parallel \mathbf{G} - \mathbf{H}]$.

Supplementary Fig. S1a also illustrates that, in general, the altermagnetic and ferromagnetic phases are always described by distinct non-relativistic spin groups. In contrast, Supplementary Fig. S1c demonstrates that the same relativistic magnetic group can, in some cases, describe both the antiparallel and parallel order of the magnetic moments. This highlights that the magnetic groups cannot, in general, discriminate between the two phases.

In Supplementary Figs. S1b,d we compare DFT calculations of Fermi surface cuts at wavevector $k_z = 0$ calculated without and with relativistic spin-orbit coupling, respectively. Even for the heavy atoms such as Ru, the spin-orbit coupling represents only a small perturbative contribution. The apparent prominent features of the relativistic Fermi surface, including the four-fold spin-momentum locking characteristic, still reflect the non-relativistic spin-group symmetries. In contrast, these prominent symmetries are omitted by the relativistic magnetic group.

In the main text, we demonstrate the electric crystal-field mechanism of the spin splitting in KRu_4O_8. Here we illustrate that this extraordinary mechanism is abundant in altermagnets with orbital degeneracies in the non-magnetic phase. In Supplementary Fig. S1e we identify the mechanism in altermagnetic RuO_2, in which earlier works reported a large spin splitting on the eV scale[3,4].

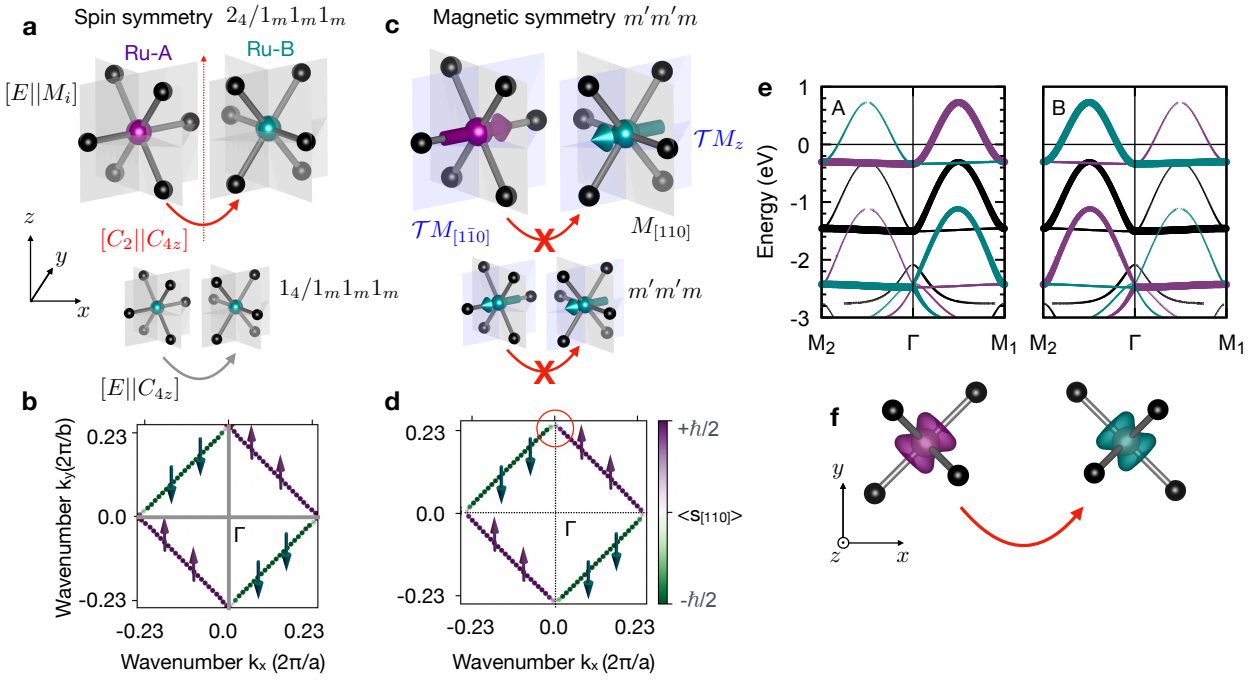

Fig. S 1. **Comparison of spin vs. magnetic group and non-relativistic vs. relativistic DFT calculation, and identification of the spin splitting by local electric crystal field in RuO_2.** **a**, Schematic spin arrangement on the RuO_2 crystal with opposite spin directions depicted by purple and cyan color, and with the depicted non-relativistic spin group. Red arrow and its label highlights the generator of opposite-spin-sublattice transformations, and the generators of the same-spin-sublattice transformations are also highlighted (in black). Bottom smaller image corresponds to the parallel spin-arrangement. **c**, Schematic spin arrangement on the RuO_2 crystal with opposite spin directions and the crystallographic spin-axis orientation depicted by purple and cyan arrows, and with the depicted relativistic magnetic group and its generators. Bottom smaller image corresponds to the parallel spin-arrangement. The crossed red arrow highlights that the magnetic group contains no opposite-spin-sublattice transformation elements. **b,d** Fermi surface cuts at wavevector $k_z = 0$ without and with relativistic spin-orbit coupling included in the DFT calculation, respectively. **e**, Projection of the non-relativistic DFT bands on the sublattice A and B $m_l = +1$ orbitals in the non-magnetic (black) and altermagnetic (purple and cyan) phase. **f**, Real-space DFT spin density around the Ru atom in sublattice A and B.

IV. COMPARISON TO RELATIVISTIC MAGNETIC GROUPS AND DFT CALCULATIONS FOR KRu_4O_8

Here we illustrate the difference between spin groups and magnetic groups on KRu_4O_8. In Supplementary Fig. S2a we recall the spin group of altermagnetic KRu_4O_8, $2_4/1_m$, and explicitly write the generators $[E \parallel \bar{E}]$ and $[E \parallel M_z]$ of the same-spin-sublattice transformations, and the generator $[C_2 \parallel C_{4z}]$ of the opposite-spin-sublattice transformations. In Supplementary Fig. S2c we give the magnetic group $2'/m'$ for the magnetic moments along the [100]-axis shown in the panel by purple and cyan arrows, and include also its generators which are the crystallographic space-inversion $\bar{E}$ and the mirror symmetry M_z, combined with time-inversion. We highlight that both these symmetry elements are same-spin-sublattice transformations and that the magnetic group contains no opposite-spin-sublattice transformation elements.

In Supplementary Figs. S2b,d we compare projections of bands on the sublattice A and B without and with spin-orbit coupling included in the DFT calculation, respectively. We see that in both cases, band states with one dominant spin projection have a dominant weight on one sublattice. (Note that the small weight on the other sublattice seen in Supplementary Fig. S2c was neglected when plotting Fig. 2f in the main text.) By comparing Supplementary Figs. S2b,d we see that the main features of the energy bands, i.e., the local electric crystal-field mechanism of the spin splitting and the spin-momentum locking are captured by the spin-group symmetries. Even for the heavy atoms such as Ru, the spin-orbit coupling represents only a small perturbative contribution. We observe the largest relativistic contributions around the $\mathbf{\Gamma}$-point, marked by the red circles. In this region the spin texture is influenced by the spin-orbit coupling which leads to a small reduction of the spin-projection along the Néel vector and a small relativistic spin splitting. The comparison of Supplementary Figs. S2b,d also demonstrates the dominant non-relativistic origin of the large spin splitting at the $\mathbf{X}$ and $\mathbf{Y}$ time-reversal invariant momenta.

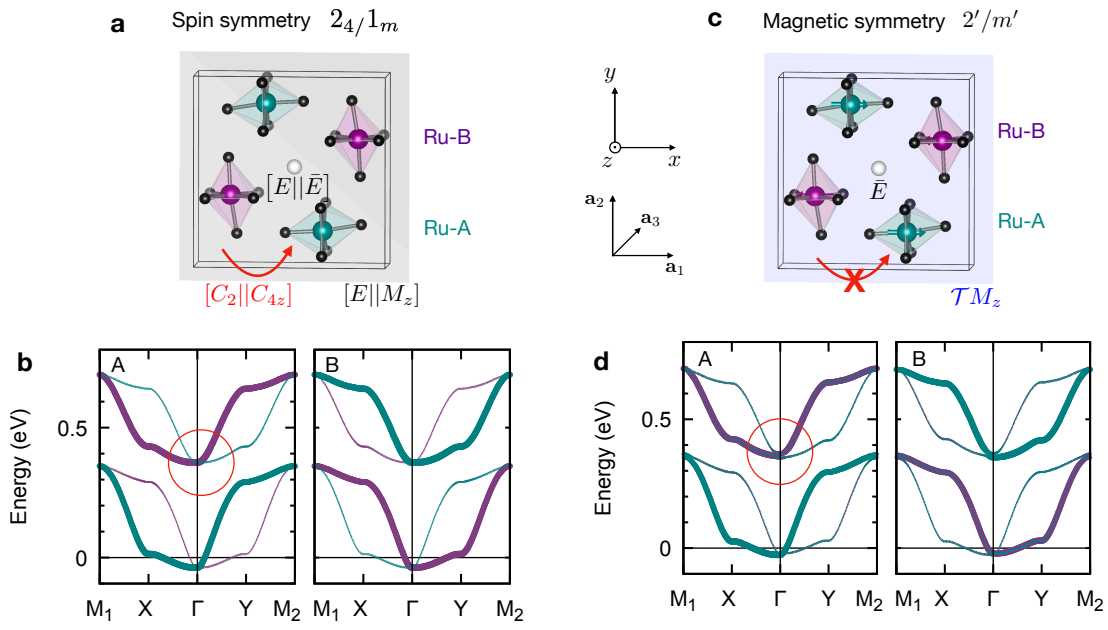

Fig. S 2. **Comparison of spin vs. magnetic group and non-relativistic vs. relativistic DFT calculation for KRu_4O_8.** **a**, Schematic spin arrangement on the KRu_4O_8 crystal with opposite spin directions depicted by purple and cyan color, and with the depicted non-relativistic spin group. Red arrow and its label highlights the generator of opposite-spin-sublattice transformations, and the generators of same-spin-sublattice transformations are also highlighted (in black). **c**, Schematic spin arrangement on the KRu_4O_8 crystal with opposite spin directions and the crystallographic spin-axis orientation depicted by purple and cyan arrows, and with the depicted relativistic magnetic group and its generators. The crossed rad arrow highlights that the magnetic group contains no opposite-spin-sublattice transformation elements. **b,d**, Projection of bands on the sublattice A and B without and with relativistic spin-orbit coupling included in the DFT calculation, respectively.

V. OTHER SELECTED ALTERMAGNETIC CANDIDATES

In this section we show DFT calculations in the altermagnetic insulator CuF_2, non-centrosymmetric altermagnet VNb_3S_6, and a parent cuprate altermagnet La_2CuO_4 of a high-temperature superconductor. Beside these materials, Tab. 1 in the main text lists also other insulating altermagnetic candidates, including high Néel temperature CoF_3 and FeF_3[20], and

semiconducting MnTe[15]. We also found altermagnetism in chalcogenite $CoNb_3S_6$[21] with bulk spin-winding number $W = 4$, or in perovskite $CaMnO_3$[22] with planar spin-winding number $W = 2$.

Altermagnetic insulator CuF_2

In Supplementary Fig. S3 we present the symmetry analysis and DFT band-structure calculations of insulating CuF_2 with the Néel temperature 69 K[23] and with relatively light elements. Its crystal, shown in Fig. S3a, is a distorted rutile with a monoclinic structure (crystal space group $P2_1/c$)[24]. The altermagnetic non-trivial spin Laue group $2_{2/}2_m$ ($[E \parallel \bar{1}] + [C_2 \parallel C_{2z}]\,[E \parallel \bar{1}]$) implies a spin winding number $W = 2$. Unlike KRu_4O_8, however, the symmetry $[C_2 \parallel M_z]$, which complements the symmetry $[C_2 \parallel C_{2z}]$, generates a bulk-like spin-momentum locking. This is confirmed by the DFT calculation presented in Fig. S3b. We used the DFT+U method with $U = 5$ eV and $J = 1$ eV to describe this Mott insulator[24]. The spin-resolved band structure is plotted in Fig. S3c. Similar to KRu_4O_8, the spin splitting is on the $\sim$100 meV scale in CuF_2. We note that the gap between the valence and conduction bands disappears for DFT with $U = J = 0$. However, within a 15% scatter, the altermagnetic spin splitting in the DFT band structure remains the same as in the Mott insulating state obtained using DFT+U. This further underlines the robustness of altermagnetism, and of the spin splitting which originates from the electro-magnetic crystal potential.

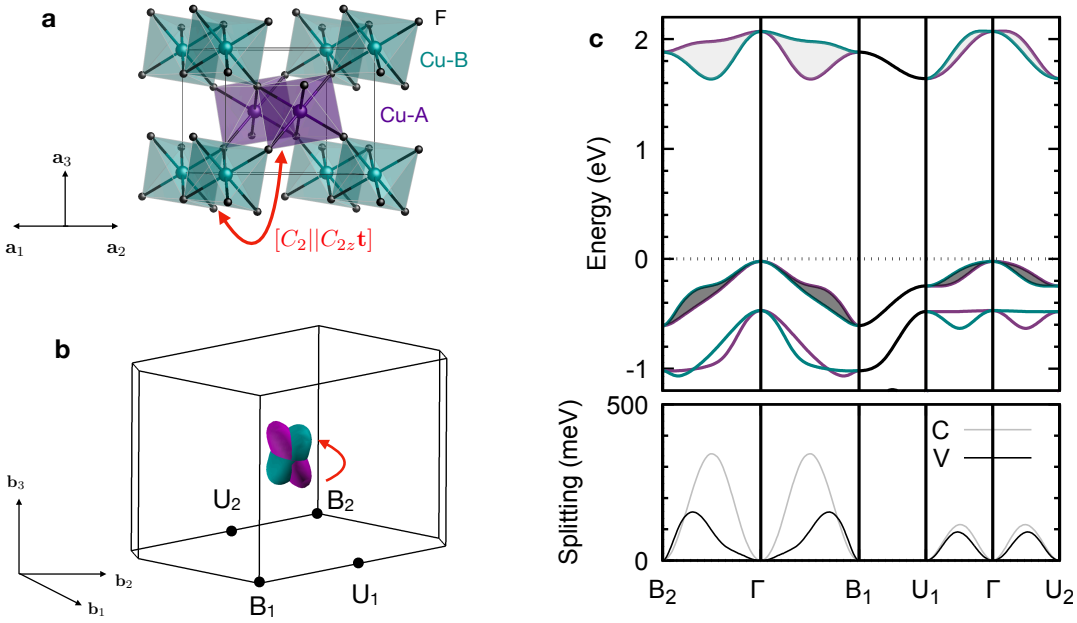

Fig. S 3. **Altermagnetic insulator CuF_2.** **a**, Schematic spin arrangement on the CuF_2 crystal with opposite spin directions depicted by purple and cyan color. Red arrow and its label highlights the opposite-spin-sublattice transformation, containing a real-space mirror or two-fold rotation (combined with real-space translation). **b**, Calculated spin-momentum locking with the bulk spin winding number $W = 2$ on top of the DFT Fermi surface for the Fermi level near the top of the valence band. **c**, DFT band structure in the altermagnetic phase. Wavevector dependence of the spin splitting between the conduction bands highlighted by the light-grey shading and valence bands highlighted by the dark-grey shading is plotted in the lower panel by light and dark lines, respectively.

Altermagnetic non-centrosymmetric VNb_3S_6

In Supplementary Fig. S4 we present the symmetry analysis and DFT band-structure calculations of non-centrosymmetric VNb_3S_6 with the Néel temperature 50 K[25]. Its non-centrosymmetric crystal[25], shown in Fig. S4a, has the crystal space group $P6_322$. The altermagnetic non-trivial spin Laue group $2_6/2_m2_m1_m$ implies bulk spin winding number $W = 4$.

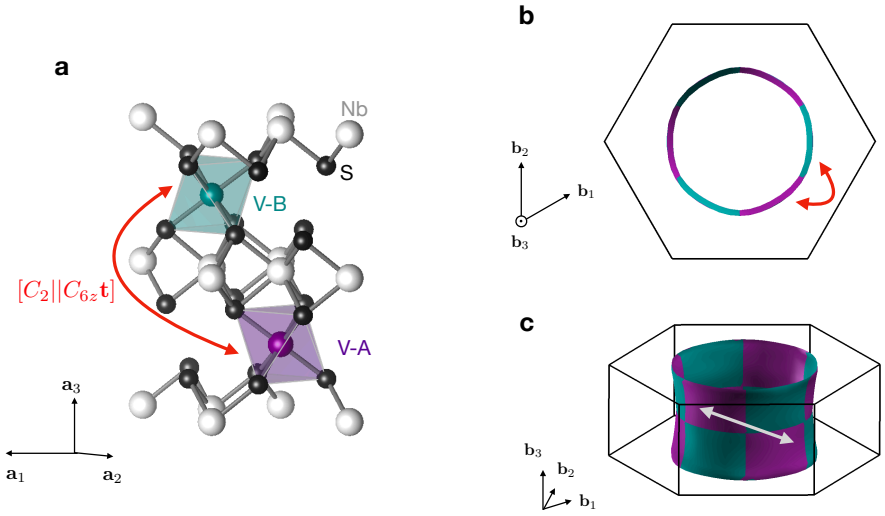

Fig. S 4. **Altermagnetic non-centrosymmetric VNb_3S_6.** **a**, Schematic spin arrangement on the VNb_3S_6 crystal with opposite spin directions depicted by purple and cyan color. Red arrow and its label highlights the opposite-spin-sublattice transformation, containing a real-space six-fold rotation. **b,c**, Calculated spin-momentum locking with the bulk spin winding number $W = 4$ on top of the DFT Fermi surface. The altermagnetic spin-momentum locking is symmetric with respect to the inversion of $\mathbf{k}$, despite the non-centrosymmetric crystal structure, as highlighted by the white double-arrow in panel c.

Altermagnetic parent cuprate La_2CuO_4 of a high-temperature superconductor

In Supplementary Fig. S5a we show the crystal structure of La_2CuO_4 in the orthorhombic phase with tilted oxygen octahedra. The spin-momentum locking in the altermagnetic phase is planar with the spin winding number $W = 2$. In literature[26], the material is known to be a metal within DFT. When including Hubbard U, we observe a Mott insulating state. However, the planar $W = 2$ altermagnetic spin-momentum locking is present in both cases.

Possible explanations why the spin-split altermagnetic phase escaped attention are that (i) previous studies focused on the high symmetry planes in the Brillouin zone, such as the grey-shaded $k_z = 0$ plane in Fig. S5b, whose spin degeneracy is protected by the spin group, or (ii) the spin splitting around the Fermi level on the ~ 10 meV scale is relatively weak.

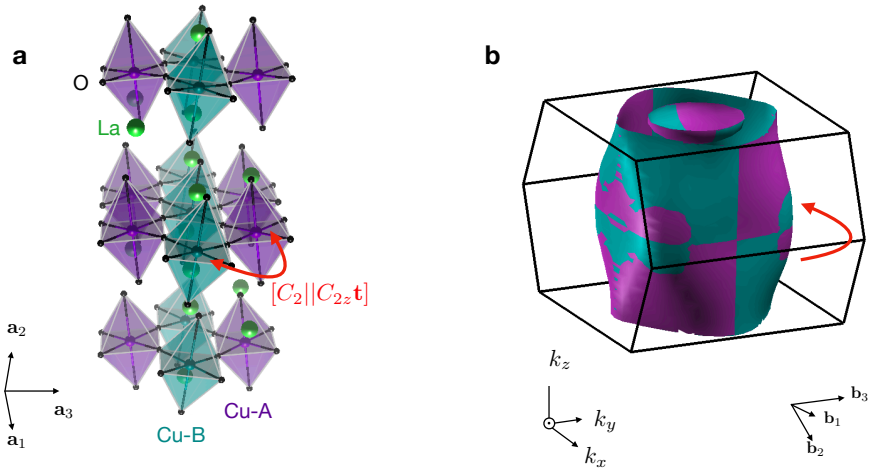

Fig. S 5. **Altermagnetic parent cuprate La_2CuO_4 of a high-temperature superconductor. a**, Schematic spin arrangement on the La_2CuO_4 crystal with opposite spin directions depicted by purple and cyan color. Red arrow and its label highlights the opposite-spin-sublattice transformation, containing a real-space two-fold rotation. **b**, Calculated spin-momentum locking with the planar spin winding number $W = 2$ on top of the DFT Fermi surface.

[1] López-Moreno, S., Romero, A. H., Mejía-López, J., Muñoz, A. & Roshchin, I. V. First-principles study of electronic, vibrational, elastic, and magnetic properties of FeF2 as a function of pressure. *Physical Review B* **85**, 134110 (2012).

[2] Noda, Y., Ohno, K. & Nakamura, S. Momentum-dependent band spin splitting in semiconducting MnO 2 : a density functional calculation. *Physical Chemistry Chemical Physics* **18**, 13294–13303 (2016).

[3] Šmejkal, L., González-Hernández, R., Jungwirth, T. & Sinova, J. Crystal time-reversal symmetry breaking and spontaneous Hall effect in collinear antiferromagnets. *Science Advances* **6**, eaaz8809 (2020).

[4] Ahn, K.-H., Hariki, A., Lee, K.-W. & Kuneš, J. Antiferromagnetism in RuO2 as d-wave Pomeranchuk instability. *Physical Review B* **99**, 184432 (2019).

[5] Hayami, S., Yanagi, Y. & Kusunose, H. Momentum-Dependent Spin Splitting by Collinear Antiferromagnetic Ordering. *Journal of the Physical Society of Japan* **88**, 123702 (2019).

[6] Naka, M. *et al.* Spin current generation in organic antiferromagnets. *Nature Communications* **10**, 4305 (2019).

[7] Yuan, L.-D., Wang, Z., Luo, J.-W., Rashba, E. I. & Zunger, A. Giant momentum-dependent spin splitting in centrosymmetric low-Z antiferromagnets. *Physical Review B* **102**, 014422 (2020).

[8] Feng, Z. *et al.* Observation of the Crystal Hall Effect in a Collinear Antiferromagnet (2020). URL `http://arxiv.org/abs/2002.08712`.

[9] Hayami, S., Yanagi, Y. & Kusunose, H. Bottom-up design of spin-split and reshaped electronic band structures in antiferromagnets without spin-orbit coupling: Procedure on the basis of augmented multipoles. *Physical Review B* **102**, 144441 (2020).

[10] Reichlova, H. *et al.* Macroscopic time reversal symmetry breaking arising from antiferromagnetic Zeeman effect. Tech. Rep. (2020). URL `https://arxiv.org/pdf/2012.15651.pdf`.

[11] Yuan, L.-D., Wang, Z., Luo, J.-W. & Zunger, A. Prediction of low-Z collinear and noncollinear antiferromagnetic compounds having momentum-dependent spin splitting even without spin-orbit coupling. *Physical Review Materials* **5**, 014409 (2021).

[12] Egorov, S. A. & Evarestov, R. A. Colossal Spin Splitting in the Monolayer of the Collinear Antiferromagnet MnF 2. *The Journal of Physical Chemistry Letters* **12**, 2363–2369 (2021).

[13] Mazin, I. I., Koepernik, K., Johannes, M. D., González-Hernández, R. & Šmejkal, L. Prediction of unconventional magnetism in doped FeSb2 (2021).

[14] Egorov, S. A., Litvin, D. B. & Evarestov, R. A. Antiferromagnetism-Induced Spin Splitting in Systems Described by Magnetic Layer Groups. *The Journal of Physical Chemistry C* acs.jpcc.1c02653 (2021).

[15] González-Hernández, R. *et al.* Efficient Electrical Spin Splitter Based on Nonrelativistic Collinear Antiferromagnetism. *Physical Review Letters* **126**, 127701 (2021).

[16] Naka, M., Motome, Y. & Seo, H. Perovskite as a spin current generator. *Physical Review B* **103**, 125114 (2021).

[17] Bose, A. *et al.* Tilted spin current generated by the collinear antiferromagnet RuO2 (2021).

[18] Šmejkal, L., Hellenes, A. B., González-Hernández, R., Sinova, J. & Jungwirth, T. Giant and tunneling magnetoresistance effects from anisotropic and valley-dependent spin-momentum interactions in antiferromagnets (2021).

[19] Shao, D.-F., Zhang, S.-H., Li, M. & Tsymbal, E. Y. Spin-neutral currents for spintronics (2021). URL `http://arxiv.org/abs/2103.09219`.

[20] Lee, S. *et al.* Weak-ferromagnetism of CoF3 and FeF3. *Physica B: Condensed Matter* **551**, 94–97 (2018).

[21] Tenasini, G. *et al.* Giant anomalous Hall effect in quasi-two-dimensional layered antiferromagnet Co1/3NbS2. *Physical Review Research* **2**, 023051 (2020).

[22] Vistoli, L. *et al.* Giant topological Hall effect in correlated oxide thin films. *Nature Physics* **15**, 67–72 (2019).

[23] Joenk, R. J. & Bozorth, R. M. Magnetic Properties of CuF 2. *Journal of Applied Physics* **36**, 1167–1168 (1965).

[24] Zheng, Y. *et al.* First-principles studies on the structural and electronic properties of Li-ion battery cathode material CuF2. *Solid State Communications* **152**, 1703–1706 (2012).

[25] Lu, K. *et al.* Canted antiferromagnetic order in the monoaxial chiral magnets ¡math xmlns. *Physical Review Materials* **4**, 054416 (2020). URL `https://journals.aps.org/prmaterials/abstract/10.1103/PhysRevMaterials.4.054416`.

[26] Lane, C. *et al.* Antiferromagnetic ground state of La2CuO4: A parameter-free ab initio description. *Physical Review B* **98**, 125140 (2018).